Spin dynamics of the block orbital-selective Mott phase

J. Herbrych[1,2],* N. Kaushal[1,2], A. Nocera[1,3], G. Alvarez[2,3], A. Moreo[1,2], and E. Dagotto[1,2]
[1] *Department of Physics and Astronomy, University of Tennessee, Knoxville, Tennessee 37996, USA*
[2] *Materials Science and Technology Division, Oak Ridge National Laboratory, Oak Ridge, Tennessee 37831, USA and*
[3] *Computational Sciences and Engineering Division and Center for Nanophase Materials Sciences, Oak Ridge National Laboratory, Oak Ridge, Tennessee 37831, USA*

(Dated: April 6, 2018)

Iron-based superconductors display a variety of magnetic phases originating in the competition between electronic, orbital, and spin degrees of freedom. Previous theoretical investigations of the one-dimensional multi-orbital Hubbard model revealed the existence of an orbital-selective Mott phase (OSMP) with block spin order, where the spins of the localized orbital form antiferromagnetically coupled ferromagnetic (FM) islands. Recent inelastic neutron scattering (INS) experiments on the quasi-1D $BaFe_2Se_3$ ladder compound confirmed the relevance of the block-OSMP. Moreover, the INS spectrum presents a rich and unexpected structure, containing low-energy *acoustic* and high-energy *optical* modes with an intensity strongly dependent on the transfered momenta. In this work we present the first theoretical study of the dynamical spin structure factor $S(q,\omega)$ within a block-OSMP regime using the density-matrix renormalization group method. In excellent agreement with experiments we find two modes: a dispersive (acoustic) mode for momentum $q < \pi/2$ and a dispersionless (optical) mode for $q > \pi/2$. We provide evidence that the former represents the spin-wave-like dynamics of the FM islands, while the latter is attributed to a novel type of local on-site spin excitations controlled by the Hund coupling.

Inelastic neutron scattering (INS) measurements are crucial for the study of quantum magnetism in condensed matter physics. This powerful experimental technique provides detailed information of momentum and energy resolved spin excitations. The importance of INS studies is best illustrated in the case of high critical temperature superconductors. Shortly after the discovery of the copper-oxide compounds it became evident that the standard BCS theory of the electron-phonon coupling could not explain the experimental findings. Simultaneously, INS results showed that superconductivity appears in close proximity to the antiferromagnetic (AFM) ordering of $S = 1/2$ Cu^{2+} moments providing robust evidence that the new pairing mechanism is based on spin fluctuations [1].

The discovery of iron-based superconductors (FeSC) added an extra complication to this "simple" picture. Although the phase diagrams of Cu-based and Fe-based materials are qualitatively similar [2], there are important conceptual differences. The most significant are in the minimal models that describe the materials [3, 4]. While cuprates have a single Fermi surface (FS), the iron-based compounds have a complicated FS with electron and hole pockets originating in the five $3d$ orbitals of iron. As a consequence, the FeSC have to be described by means of multi-orbital Hubbard models, involving not only a standard Hubbard U repulsion but also a Hund coupling. The competition between electronic, orbital, and spin degrees of freedom can lead to many exotic magnetic phases [5–10].

Past experience in cuprates showed that the analysis of lower dimensional systems, such as chains and ladders, can provide useful information to better contrast theory with experiments [11]. One reason is that theoretical many-body calculations based on model Hamiltonians can be accurately performed in one dimension, particularly numerically. For this reason, it was exciting when a one-dimensional family of compounds containing two-leg ladders was unveiled also in the iron-superconductors context. Specifically, we refer to the low-dimensional FeSC in the 123 family, AFe_2X_3, where A are alkali metals A=K, Ba, Rb, Cs, and X are chalcogenides X=S, Se. These compounds are build of double chains (i.e. they are ladders) of edge sharing FeX_4 tetrahedra [12]. Recently, a superconducting state was identified under pressure for $BaFe_2S_3$ [13, 14] and $BaFe_2Se_3$ [15, 16]. The pressure-dependent phase diagram of these materials resembles that of copper-oxide ladders, e.g., the *telephone number* compound $Sr_{14-x}Ca_xCu_{24}O_{41}$ [17]. Similar to their copper oxide counterparts, the iron-123 family is insulating at ambient pressure. This behavior is unusual since, unlike the cuprates, the parent compounds of FeSC are typically bad metals. In addition, it was argued that orbital-selective Mott physics (OSMP) [18] is consistent with results for $BaFe_2Se_3$ [19–22]. Within such a phase, itinerant and localized conduction electrons coexist.

It should be remarked that INS experiments on 123 materials have been performed up to now only on *powder* samples and, as a consequence, detailed data of the momentum dependence of the spin excitations over the whole Brillouin zone is not yet available. Nevertheless, the static $(\pi, 0)$ stripe AFM order – with ferromagnetic rungs and antiferromagnetic legs – was identified for $BaFe_2S_3$ [23], $RbFe_2Se_3$ [24], $CsFe_2Se_3$ [25, 26], and also for KFe_2S_3 [19]. However, in the special case of $BaFe_2Se_3$ remarkably an exotic block magnetism was found [16, 19, 22, 27, 28] involving antiferromagnetically coupled ferromagnetic islands made of 2×2 iron clusters.

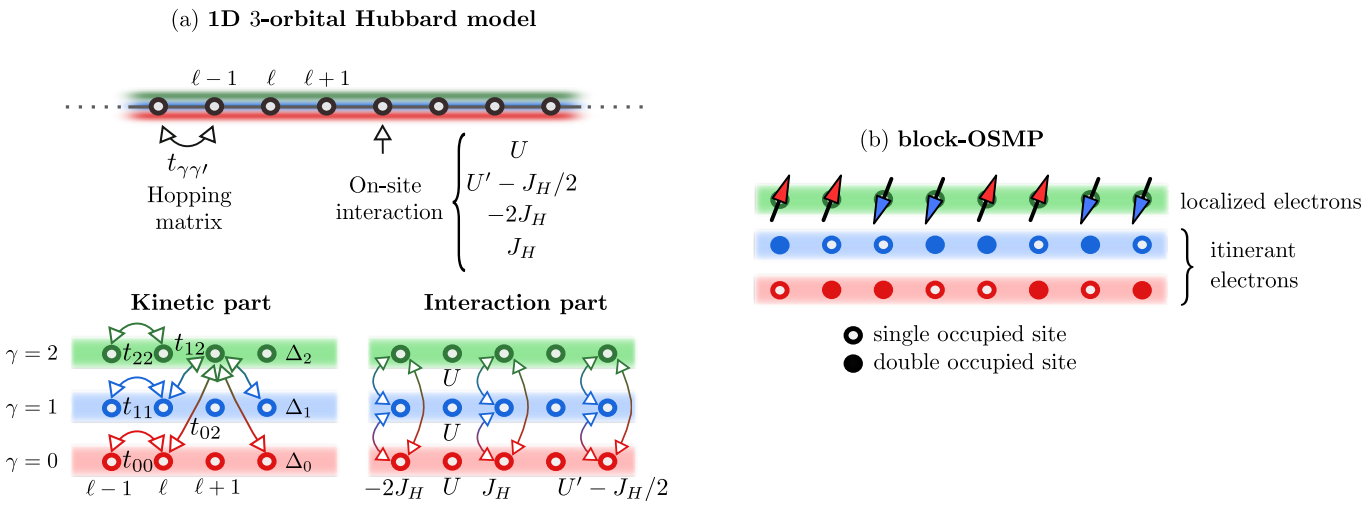

Figure 1. **Schematic representation of the Hamiltonian considered in this work.** (a) Three-orbital Hubbard model on a one-dimensional lattice geometry (see text for details). (b) Schematic representation of the block orbital selective Mott phase. The pattern of single and double occupied sites in the itinerant electrons is meant to be random, representing pictorially the not-localized nature of those orbitals.

This unusual magnetic state was also observed in the vicinity of superconductivity [29–31] in two-dimensional (2D) materials with $\sqrt{5}\times\sqrt{5}$ ordered iron vacancies, such as $Rb_{0.89}Fe_{1.58}Se_2$ [32] and $K_{0.8}Fe_{1.6}Se_2$ [33]. In addition, for $BaFe_2Se_3$ [22], $BaFe_2S_3$ [23], and $RbFe_2Se_3$ [24] the INS revealed the existence of low-energy acoustic and high-energy optical modes separated by an energy gap, although their origin and characteristics were not clarified.

In this work, we will address the spin dynamical properties of the exotic block magnetic state found in $BaFe_2Se_3$. The static (time independent) properties of this phase were previously qualitatively studied in Ref. [20] via a three-orbital Hubbard model in one-dimension (1D) that unveiled an OSMP regime. Here, we will use the same Hamiltonian to investigate the momentum and energy resolved spin dynamics. To test the general features of our findings we present also results obtained in a quasi-1D ladder geometry. To the authors knowledge, these are the first numerically-exact electronic calculations of the dynamical spin structure factor in a multi-orbital Hubbard model. In agreement with experimental findings we have observed two distinct modes of spin excitations: a low-energy dispersive mode and high-energy dispersionless optical modes. The low-energy acoustic mode reveals the frustrated nature of the block magnetism which can be described by a spin J_1-J_2 Hamiltonian. Moreover, we argue that the optical mode is controlled by local orbital physics and it cannot be properly captured by a Heisenberg-like model. The main features of our analysis are simple and generic and should characterize any multi-orbital model as long as its ground state is in a magnetic block phase.

RESULTS

Model and observables. We will focus on a specific three-orbital Hubbard model on a one-dimensional lattice, but our conclusions are generic for a broad group of models and materials in the OSMP magnetic block-phase regime. As mentioned before, the model chosen was previously studied with regards to its time-independent properties, and it is known that it displays an OSMP regime in the ground state [20]. The kinetic part of the Hamiltonian, $H_{\rm kin}$, is defined as:

$$H_{\rm kin} = \sum_{\ell,\sigma,\gamma,\gamma'} t_{\gamma\gamma'} \left(c^\dagger_{\ell,\gamma,\sigma} c_{\ell+1,\gamma',\sigma} + \text{H.c.} \right) + \sum_{\ell,\gamma,\sigma} \Delta_\gamma n_{\ell,\gamma,\sigma} \,, \tag{1}$$

where $c^\dagger_{\ell,\gamma,\sigma}$ creates an electron with spin $\sigma = \{\uparrow,\downarrow\}$ at orbital $\gamma = \{0,1,2\}$ and site $\ell = \{1,\ldots,L\}$ of a 1D chain. $n_{\ell,\gamma,\sigma} = c^\dagger_{\ell,\gamma,\sigma} c_{\ell,\sigma,\gamma}$ is the local (ℓ,γ) electron density with spin σ. Note that another common labeling of these orbitals could be based on the canonical t_{2g} manifold, i.e. $\{yz\,, xz\,, xy\}$, respectively. $t_{\gamma\gamma'}$ denotes a symmetric hopping amplitude matrix defined in the orbital space γ: $t_{00} = t_{11} = -0.5$, $t_{22} = -0.15$, $t_{02} = t_{12} = 0.1$ and $t_{01} = 0$, all in eV units [Fig. 1(a) displays a schematic representation of the Hamiltonian]. The crystal-field splitting is set to $\Delta_0 = -0.1$, $\Delta_1 = 0$, and $\Delta_2 = 0.8$, also in eV units. The total kinetic-energy bandwidth is $W = 2.45\,$eV. These phenomenological values of parameters were chosen before [20] to reproduce qualitatively the band structure properties of higher dimensional selenides at an electronic density $\overline{n} = 4/3$ per orbital, namely an electron-like pocket at $k = 0$ and hole-like pockets at $k = \pm\pi$ (see Ref. [34] and references therein). However, again, we emphasize that our predic-

tions below are believed to be universal and primarily depend on the existence of an OSMP block-phase state, rather than on the details of the Hamiltonian that leads to its stabilization. In order to support this claim, we will present calculations for several models, and all the results lead essentially to the same qualitative conclusions.

The interaction portion of the Hamiltonian $H_{\rm int}$ is given by

$$H_{\rm int} = U \sum_{\ell,\gamma} n_{\ell,\gamma,\uparrow} n_{\ell,\gamma,\downarrow} + (U' - J_H/2) \sum_{\ell,\gamma<\gamma'} n_{\ell,\gamma} n_{\ell,\gamma'} - 2J_H \sum_{\ell,\gamma<\gamma'} S_{\ell,\gamma} S_{\ell,\gamma'} + J_H \sum_{\ell,\gamma<\gamma'} \left(P^+_{\ell,\gamma} P_{\ell,\gamma'} + \text{H.c.} \right), \quad (2)$$

where $n_{\ell,\gamma} = \sum_\sigma n_{\ell,\gamma,\sigma}$, the local spin (ℓ,γ) is $S_{\ell,\gamma} = \sum_{a,b} c^\dagger_{\ell,\gamma,a} \sigma^{ab} c_{\ell,\gamma,b}$ (with σ^{ab} as a Pauli spin matrices), and $P_{\ell,\gamma} = c_{\ell,\uparrow,\gamma} c_{\ell,\downarrow,\gamma}$ is the pair-hopping. We will consider an SU(2) symmetric system, i.e. $U' = U - 2J_H$, where U stands for the on-site same-orbital repulsive Hubbard interaction. Finally, we set the Hund coupling to $J_H = U/4$, a value widely used before and considered to be realistic for Fe-based materials [35, 36]. We refer the interested reader to Refs. [20, 37, 38] for details of the J_H-U phase diagram of the above Hamiltonian. Here, if not stated differently, we will use $U/W = 0.8$ where previous studies found [20] a block-OSMP , i.e. antiferromagnetically (AFM) coupled ferromagnetic (FM) blocks (magnetic unit cells), $\uparrow\uparrow\downarrow\downarrow\uparrow\uparrow\downarrow\downarrow$, in the localized orbital $\gamma = 2$ [see Fig. 1(b)]. Note that the block order in our system is an effect of the electronic correlations and not of the dimerization, like is the case in the spin-wave description of the experiment [22, 32]. The Hamiltonian is diagonalized via the DMRG method, where the dynamical correlation functions are obtained with the help of dynamical-DMRG techniques (see Methods and Supplemental Material [39] for details of the numerical simulations).

In this work, we will investigate the zero-temperature frequency ω-dependent spin structure factor (SSF) $S(q,\omega)$, defined as the Fourier transform of the real-space total (on-site, $S_\ell = \sum_\gamma S_{\ell,\gamma}$) spin correlation functions (see Methods). Furthermore, we will study the contributions from the individual orbitals to the total SSF, i.e. $S_{\gamma\gamma'}(q,\omega)$. $\gamma = \gamma'$ denotes the spin fluctuations within each of the orbitals, while $\gamma \neq \gamma'$ are spin fluctuations between different orbitals. As a consequence $S(q,\omega) = \sum_\gamma S_{\gamma\gamma}(q,\omega) + \sum_{\gamma\neq\gamma'} S_{\gamma\gamma'}(q,\omega)$. From the experimental perspective, note that only the total SSF has a meaning [40] because neutrons couple to electrons in all orbitals in neutron scattering experiments. On the other hand, the theoretical investigations of orbital-resolved SSF can provide further insight into the OSMP physics.

Dynamical spin structure factor. In Fig. 2 we present one of the main results of our effort: the frequency-momentum dependence of the dynamical SSF

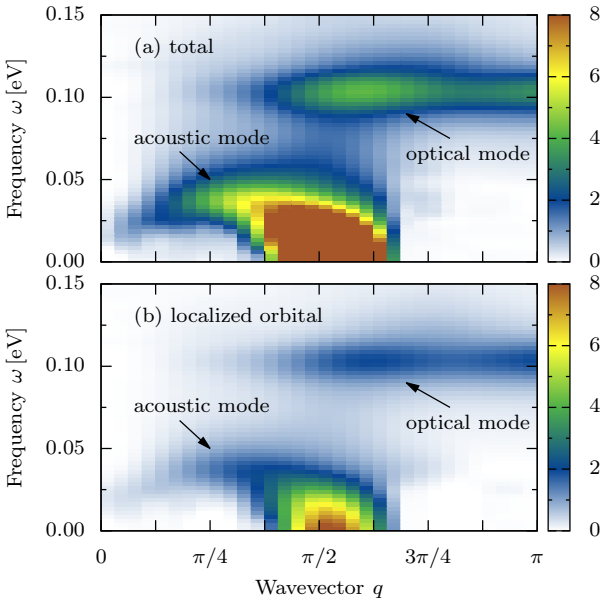

Figure 2. **Dynamical spin structure factor (SSF) within the block-OSMP phase.** (a) Total SSF, $S(q,\omega)$, and (b) SSF of the localized orbital, $S_{22}(q,\omega)$. Both results exhibit a low-energy acoustic and a high-energy optical modes. Note that the spectral weight of the localized orbital, S_{22}, constitutes $\sim$ 50% of the total SSF weight. The results were obtained using a dynamical-DMRG method with parameters $L = 16$ (48 orbitals), $M = 800$, $\delta\omega = 0.005\,$eV, and $\eta/\delta\omega = 2$.

in the block-OSMP phase (i.e. at $U/W = 0.8$). Panel (a) depicts the total SSF, $S(q,\omega)$, while panel (b) shows only the contribution from the localized orbital, $S_{22}(q,\omega)$. Several conclusions can be obtained directly from the presented results: (i) A robust contribution to the total SSF arises from the localized orbital. Moreover, all the qualitative features of $S(q,\omega)$ are already present in $S_{22}(q,\omega)$. In fact, $S(q,\omega)$ and $S_{22}(q,\omega)$ become almost indistinguishable [see Fig. 5(a) later] if normalized by the local magnetic moment squared (i.e. $S^2 = 3/4$ for the $S = 1/2$ localized electron, and $S^2 = 2$ for the total moment [20]). (ii) The energy range for the spin dynamics is much smaller when compared with the energy bandwidth $W = 2.45\,$eV of the Hamiltonian. (iii) Clearly the dynamical SSF has two distinct modes: a low-frequency, $\omega \lesssim \omega_c = 0.08\,$eV, dispersive (*acoustic*) band and a high-frequency, $\omega \sim 0.11\,$eV, dispersionless (*optical*) band. Similar results were previously reported experimentally in INS investigations of $BaFe_2Se_3$ [22] (with 2×2 FM blocks), $BaFe_2S_3$ [23] and $RbFe_2Se_3$ [24] (with 2×1 FM blocks). The different types of blocks in the INS investigations, and the similarity of results between neutrons and our calculations, suggest that our results apply to a broad variety of iron chalcogenides. Moreover, the INS measurements where performed on powder samples and, as a consequence, no detailed analysis of the spin

excitations over all crystal momenta q (over the whole Brillouin zone) have been reported. In this respect, our results define clear theoretical predictions on what future single-crystal experiments should display.

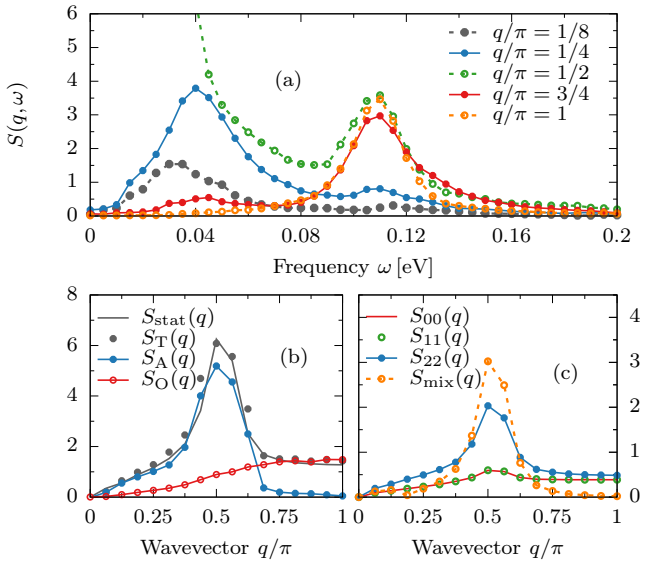

Figure 3. **Frequency and momentum dependence of the SSF.** (a) Finite momentum cuts, $q/\pi = 1/8, 1/4, 1/2, 3/4, 1$, of the dynamical SSF. (b) Total static SSF obtained as an expectation value in the $|\mathrm{GS}\rangle$, $S_{\rm stat}(q)$ (black line), and also via the ω integration of the dynamical SSF, $S_{\rm T}(q)$ (black points). In the same panel we present also the contributions to the static SSF from acoustic and optical modes, $S_{\rm A}(q)$ and $S_{\rm O}(q)$, respectively. (c) Contribution to the static SSF $S_{\gamma\gamma'}(q)$: $\gamma = \gamma'$ represents the SSF component for each of the orbitals, while $S_{\rm mix}(q) = \sum_{\gamma\neq\gamma'} S_{\gamma\gamma'}(q)$ represents the sum of the inter-orbital contributions. The system parameters are the same as in Fig. 2.

In Fig. 3(a) we present the ω dependence of the total SSF at special values of the momenta q. It is evident that the acoustic mode is strongly momentum dependent in the range $0 < q/\pi \lesssim 1/2$, while it reduces drastically its intensity for $q/\pi > 1/2$. To understand these results, we can reanalyze the SSF spectrum using two-sites as a rigid block, namely creating an effective *magnetic* unit cell of FM-blocks with momentum $\widetilde{q}$. The acoustic mode as a function of $\widetilde{q}$ then is located between $0 < \widetilde{q} < \pi$, resembling a gapless continuum of spin excitations. Such an interpretation is consistent with "collective" spin waves based on FM blocks. On the other hand, the high-energy optical contribution is q-independent for $q/\pi \gtrsim 1/2$, with vanishing intensity in the $q \to 0$ limit. As discussed later, this mode can be associated to local (on-site) spin excitations affecting the Coulomb potential portion of the Hamiltonian, independently of the dimensionality of the system. The q-dependence of both modes is also clearly visible in the static SSF obtained from the energy integration of the dynamical SSF, i.e. $S_\alpha(q) = (1/\pi)\int \mathrm{d}\omega\, S(q,\omega)$. In Fig. 3(b) we present the acoustic ($\alpha = \mathrm{A}$) and optical ($\alpha = \mathrm{O}$) contribution to the total ($\alpha = T$) static SSF, coming from the integration over the frequency ranges $0 < \omega < \omega_c$, $\omega_c < \omega < \infty$, and $0 < \omega < \infty$, respectively. From the dynamical SSF spectra, it is evident that $S_{\rm O}(q)$ provides the sole contribution to the total static SSF for momentum $0.75 < q/\pi < 1$. As a consequence, at least within a block-OSMP state it is remarkable that already in the static SSF one can observe the clear presence of an optical mode, a novel result which is intrinsic of block phases. In the same panel, we also present the total static SSF independently obtained from the expectation value of the ground state (GS), i.e., $S_{\rm stat}(q) = \langle \mathrm{GS}|S_q \cdot S_{-q}|\mathrm{GS}\rangle$, where S_q is the Fourier transform of the S_ℓ operators for the same system size L. The agreement between $S_{\rm stat}(q)$ and $S_{\rm T}(q)$ serves as nontrivial accuracy test of the dynamical-DMRG method, since the former can be obtained with much higher accuracy.

Orbital contribution. Before addressing the optical and acoustic modes in more detail, we will comment on the orbital γ contribution to $S(q,\omega)$. As already shown in Fig. 2, the main contribution to the total SSF originates in the localized orbital $\gamma = 2$. Our results [see Fig. 3(c)] indicate that the spin fluctuations for the itinerant electrons (orbitals $\gamma = 0$ and $\gamma = 1$) follow the behavior of the localized orbital. As argued below, this is a consequence of the Hund coupling which aligns ferromagnetically spins at different orbitals. However, the nature of these orbitals is metallic and magnetic moments are not well formed. As a consequence, the spectral weight of the total itinerant contribution (2 orbitals) is approximately the same as the localized (1 orbital). On the other hand the inter-orbital SSF $S_{\gamma\neq\gamma'}$ have a large contribution only to the acoustic mode, especially near the $q/\pi = 1/2$ point.

Acoustic mode. Consider now the properties of the acoustic mode. Motivated by the results presented above, with the main contribution to the SSF arising from the localized orbital, we express the eigenstates in terms of the basis states of localized orbital $|\cdot\rangle_{\gamma=2}$ (see Methods section). Since the electrons are indeed localized with occupation $n_{\gamma=2} = 1$ [20] in the OSMP, in the low-energy portion of the spectrum the basis states with empty and double occupied orbital $\gamma = 2$ should not be present. Within such a representation the GS of the block-OSMP phase can be identified as a superposition of $|\uparrow\uparrow\downarrow\downarrow\rangle_{\gamma=2}$ and $|\downarrow\downarrow\uparrow\uparrow\rangle_{\gamma=2}$ states which constitutes $\sim 50\%$ of the true GS. One can improve further the qualitative description by investigating a simple toy model. Let us consider two FM coupled $S = 1/2$ spins as one $S = 1$ object, i.e. $|\mathbf{1}\rangle = |\uparrow\uparrow\rangle_{\gamma=2}$, $|-\mathbf{1}\rangle = |\downarrow\downarrow\rangle_{\gamma=2}$, and $|\mathbf{0}\rangle = 1/\sqrt{2}(|\uparrow\downarrow\rangle_{\gamma=2} + |\uparrow\downarrow\rangle_{\gamma=2})$. In this setup, a 4-site $S = 1/2$ system reduces to two antiferromagnetically coupled $S = 1$ spins. The ground state of the latter is

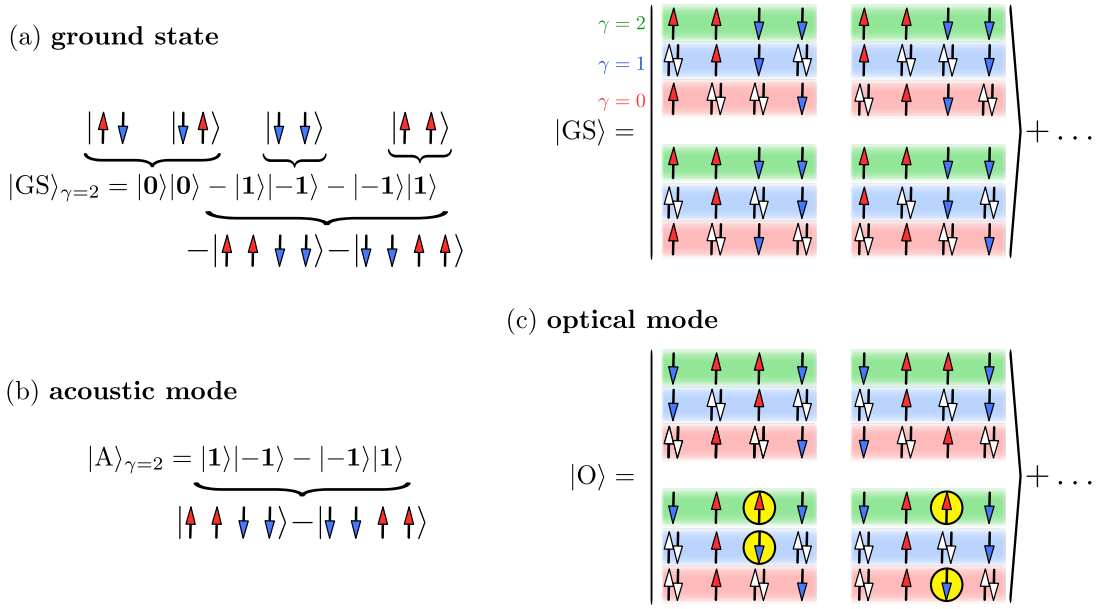

Figure 4. **Schematic representation of the states relevant for the dynamical SSF.** Spin configuration in the localized orbital ($\gamma = 2$) (see text for details) of the (a) $|\mathrm{GS}\rangle$ (singlet) and (b) $|\mathrm{A}\rangle$ state (triplet) contributing to the acoustic mode. (c) Schematic representation of particle configuration of all orbitals of the $|\mathrm{GS}\rangle$ and optical triplet $|\mathrm{O}\rangle$. Circles represent pairs of antiferromagnetically aligned spins which break the Hund's rule.

simply

$$|\mathrm{GS}\rangle_{\gamma=2} = c_a|\mathbf{0}\rangle|\mathbf{0}\rangle - c_b\Big(|\mathbf{1}\rangle|-\mathbf{1}\rangle + |-\mathbf{1}\rangle|\mathbf{1}\rangle\Big)\,, \qquad (3)$$

where $c_a = c_b = 1/\sqrt{3}$ [see Fig. 4(a) for a schematic representation]. Note that the above state, in agreement with numerics, is a singlet. The last two terms of Eq. 3 correspond to the "perfect" block order, i.e., $|\uparrow\uparrow\downarrow\downarrow\rangle_{\gamma=2} + |\downarrow\downarrow\uparrow\uparrow\rangle_{\gamma=2}$, while the first term depicts the chiral nature of the block order,

$$|\mathbf{0}\rangle|\mathbf{0}\rangle = \frac{1}{2}\Big(|\uparrow\downarrow\uparrow\downarrow\rangle_{\gamma=2} + |\downarrow\uparrow\downarrow\uparrow\rangle_{\gamma=2} + |\uparrow\downarrow\downarrow\uparrow\rangle_{\gamma=2} + |\downarrow\uparrow\uparrow\downarrow\rangle_{\gamma=2}\Big)\,. \qquad (4)$$

Our $L = 4$ Lanczos investigation of the full Hamiltonian (1-2) indicates that such a state has coefficients equal to $\widetilde{c}_a^2 \simeq 1/6$ and $\widetilde{c}_b^2 \simeq 1/4$, which yields now a better overlap, $\sim 70\%$, with the true GS. Finally, the first excited state - contributing to the acoustic mode - can be identified as a triplet of the form $|\mathrm{A}\rangle_{\gamma=2} = \widetilde{c}_A(|\uparrow\uparrow\downarrow\downarrow\rangle_{\gamma=2} - |\downarrow\downarrow\uparrow\uparrow\rangle_{\gamma=2})$ where $\widetilde{c}_A^2 \simeq 4/9$ [see Fig. 4(b)]. This large overlap of $|\mathrm{A}\rangle_{\gamma=2}$ with the full solution is also captured by the toy model since $|\mathbf{1}\rangle|-\mathbf{1}\rangle - |-\mathbf{1}\rangle|\mathbf{1}\rangle$ is one of the first excitations in our two-site $S = 1$ problem. Note that the above description of the $|\mathrm{GS}\rangle_{\gamma=2}$ ($|\mathrm{A}\rangle_{\gamma=2}$) as a spin singlet (triplet) is not obvious from the signs of the localized orbital basis representation. While the above states capture the essence of the problem, the itinerant orbitals have to be included in the description to account for the true nature of the singlet-triplet excitation.

Although simplified, descriptions such as those above of the low-energy spectrum can yield nontrivial consequences. A similar ground state to our $|\mathrm{GS}\rangle_{\gamma=2}$ with $\pi/2$ *pitch angle* was previously observed in the frustrated ferromagnetic $S = 1/2$ J_1–J_2 Heisenberg model with ferromagnetic J_1 and antiferromagnetic J_2 [41–45]. In Fig. 5(a) we present a comparison of the multi-orbital system Eqs. (1-2) SSF vs J_1-J_2 results obtained for $J_2/|J_1| = 1$. Within the latter the dynamical SSF yields a continuum of excitations with maximum intensity at $q/\pi = 1/2$ and vanishing intensity in the $q/\pi \to 1$ limit. In fact, the dynamical SSF of the J_1–J_2 model is very similar to the acoustic mode found in our multi-orbital system, i.e. compare panels (b) and (c) of Fig. 5. To strengthen this argument, in Fig. 5(b,c) we present the dynamical SSF factor plotted against the quantum dispersion relation of the J_1–J_2 model $\omega(q) = \epsilon_q - \epsilon_{\mathrm{GS}}$ where ϵ_q is the energy of the lowest eigenstate at a given q. To match the energy scales we set $|J_1| = J_2 = 0.6J_{\mathrm{eff}}$ where $J_{\mathrm{eff}} = 4\,t_{22}^2/U$ is the *natural* superexchange scale within the localized orbital, as a crude approximation. As clearly shown in Fig. 5(b), $\omega(q)$ quantitatively captures the main features of the acoustic portion of the spectrum.

It should be pointed out that the present comparison with the J_1–J_2 model is at a phenomenological level, since this effective description of the lowest mode of the spin dynamics was not rigorously derived from our multi-orbital Hamiltonian Eqs. (1-2). The acoustic mode reflects the frustrated nature of the magnetism

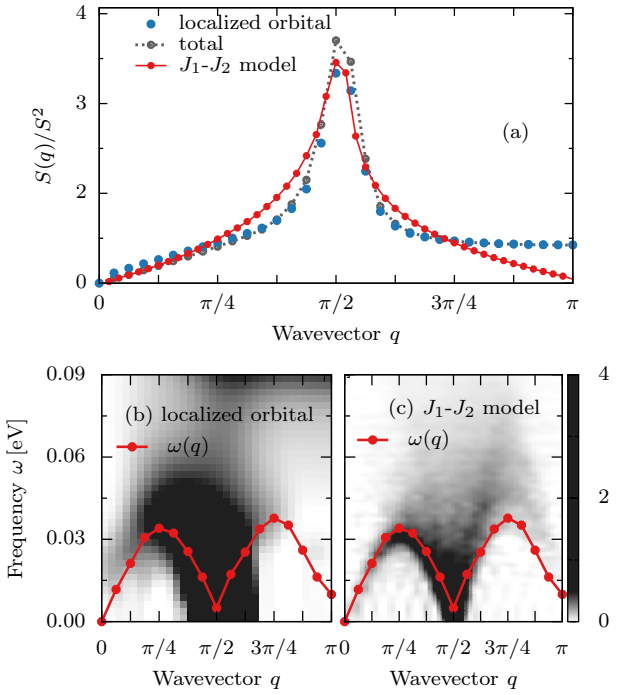

Figure 5. **Comparison with the J_1–J_2 model.** (a) Comparison of the static SSF $S(q)$ corresponding to the multi-orbital system vs results for the J_1–J_2 model with $J_2/|J_1| = 1$, calculated for $L = 32$ and $L = 48$, respectively. $S(q)$ is normalized by the local magnetic moment squared $S^2 = S(S+1)$, where $S^2 = 3/4$ for the localized orbital and the J_1–J_2 result, and $S^2 = 2$ [20] for the total SSF. (b) Acoustic mode of the dynamical SSF within the block-OSMP phase (the same results as in Fig. 2(b)) compared against the dispersion relation $\omega(q)$ of the J_1–J_2 model with $|J_1| = J_2 = 0.6J_{\rm eff}$, where the effective spin exchange energy scale is set to $J_{\rm eff} = 4\,t_{22}^2/U$. The latter is obtained with the help of Lanczos diagonalization on a chain of 32 sites with periodic boundary conditions. (c) Dynamical SSF of the J_1–J_2 model with $|J_1| = J_2 = 0.6J_{\rm eff}$ as calculated using DMRG for a $L = 48$ chain.

within the block-OSMP phase. Also, the J_1–J_2 model is probably relevant in a wide range of interaction U in the OSMP phase, beyond the block ordering region $0.4 \lesssim U/W \lesssim 1.5$. Previous results show that for interaction strength $1.5 \lesssim U/W \lesssim 20$ the system is in the ferromagnetic-OSMP [20], where all the spins within the localized orbital $\gamma = 2$ have ferromagnetic ordering. It is clear that a J_1–J_2 model with small or vanishing J_2 will also exhibit a similar ordering. Finally, although the alternative $S = 1$ toy model is useful in the description of elementary states of the block-OSMP system, its validity is limited for the dynamical spin response: it is well known that the dynamical SSF of the $S = 1$ AFM Heisenberg model exhibits "sharp" magnon lines, in contrast to the $S(q,\omega)$ of the $S = 1/2$ model that contains a continuum of excitation (at least at low-ω), in agreement with our findings for the three-orbital Hamiltonian.

Optical mode. Let us now turn to the high-energy optical mode of the dynamical SSF spectrum. The states contributing to this mode are also triplet excitations. In the $L = 4$ Lanczos analysis we found that this high-energy mode arises from a state of the form $|\mathrm{O}\rangle_{\gamma=2} \simeq 1/2(|\downarrow\uparrow\uparrow\downarrow\rangle_{\gamma=2} + |\uparrow\downarrow\downarrow\uparrow\rangle_{\gamma=2})$ [46]. It is evident that $|\mathrm{O}\rangle$ breaks the FM magnetic unit cells present in the GS. Note, again, that the discussed states do not have doubly occupied or empty sites, reflecting the Mott nature of orbital $\gamma = 2$.

To understand properly the optical mode it is not enough to focus solely on the localized orbital. A detailed analysis of the remaining "metallic" orbitals $\gamma = 0, 1$ indicates that: (i) the $|\mathrm{GS}\rangle$ and the $|\mathrm{A}\rangle$ states obey the Hund's rule: spins in different orbitals of the same site are ferromagnetically aligned [see Fig. 4(a) for a schematic representation]. (ii) However, the $|\mathrm{O}\rangle$ states, Fig. 4(c), do not fulfill this rule because part of the spins are antiferromagnetically aligned. As a consequence, the main difference in energy between the $|\mathrm{GS}\rangle$ and $|\mathrm{O}\rangle$ arises from the local (on-site) Hund exchange portion of the electronic interaction. We confirm this by calculating separately the expectation values of all terms contributing to the Hamiltonian (see Methods section). The main difference between the energy of the $|\mathrm{GS}\rangle$ and $|\mathrm{A}\rangle$ arises from the kinetic portion. On the other hand, the difference in $|\mathrm{O}\rangle$ originates, as expected, from the Hund coupling part of the interaction energy. The local on-site nature of the optical mode is also visible in the orbital resolved SSF. In Fig. 3(c) we present the spin correlations between different orbitals at different sites, i.e. $S_{\rm mix}$. As clearly visible, the $S_{\rm mix}(q \to \pi) \to 0$, indicating a drastic reduction of spectral weight at large momentum. These findings indicate that the optical mode is not present in the inter-orbital inter-site spin correlations. As a consequence, the only remaining possibility of the origin of the optical mode are the intra-site fluctuations between orbitals. Our investigation of orbital resolved SSF [see Fig. 3(c)] shows that each orbital contributes to the optical mode with a similar weight. Finally, the lack of momentum dependence of the optical mode (at least for $q/\pi > 1/2$) suggests that such excitations are local (on-site) fluctuations of spin between different orbitals at the same site.

In addition, we have shown that the frequency $\omega_{\rm O} = \epsilon_{\rm O} - \epsilon_{\rm GS}$ of the corresponding $|\mathrm{O}\rangle$ excitation is directly proportional to the value of the Hund exchange J_H, contrary to the $|\mathrm{A}\rangle$ excitation with energy $\omega_{\rm A} = \epsilon_{\rm A} - \epsilon_{\rm GS}$. In Fig. 6(a) we present the dynamical SSF at $q/\pi = 1/2$ for various values of U within the block-OSMP calculated via the Lanczos method on $L = 4$ sites, at a fixed $J_H/U = 1/4$. Our results in Fig. 6(b) indicate that this behavior is valid throughout the entire block-OSMP phase, $0.4 \lesssim U/W \lesssim 1.5$.

Ladder geometry. Finally, let us comment on the lattice geometry dependence of our results. In Fig. 7 we

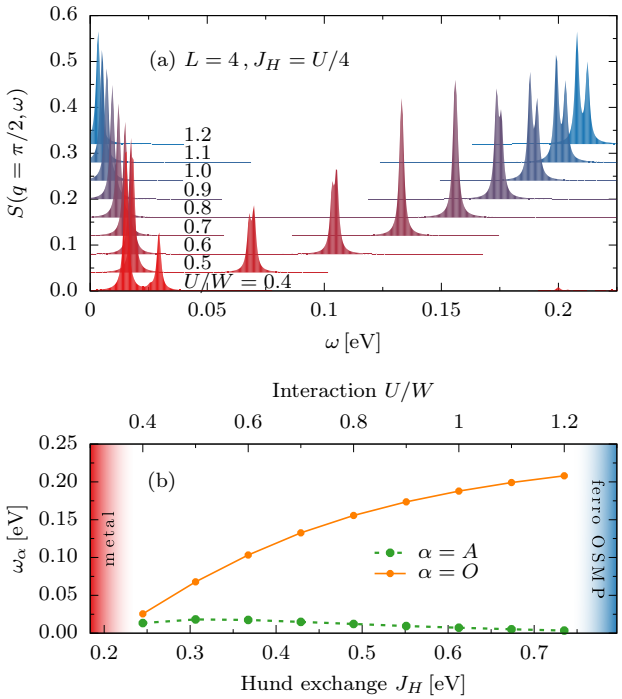

Figure 6. **Hund exchange dependence of the SSF modes.** (a) Dynamical SSF at $q/\pi = 1/2$ for various values of the interaction U, all within the block-OSMP phase, $U/W = 0.4, \ldots, 1.2$ (bottom to top, with 0.04 offset), at a fixed $J_H/U = 1/4$, calculated for $L = 4$ using the Lanczos method. (b) Frequency $\omega_\alpha = \epsilon_\alpha - \epsilon_{\rm GS}$ dependence of the acoustic and optical modes vs the value of the Hund exchange coupling J_H.

present the SSF for the two-leg ladder two-orbital Hamiltonian introduced in Ref. [34] for the $BaFe_2Se_3$ compound. The lattice is sketched in Fig. 7(a) and hopping values are given in the Methods section. It was previously shown [34] that at density $\overline{n} = 1.75/2$, $J_{\rm H} = U/4$, and $U/W_L = 2$ with $W_L = 3.82\,$eV the system is in an enlarged block phase, similar to the 2×2 block state of $BaFe_2Se_3$ [22]. Before addressing specific results, it is important to remark that the DMRG numerical studies of multi-orbital ladders require expensive computations. This is because the inter-site inter-orbital hoppings behave effectively as long-distance hoppings in the equivalent one-dimensional representation, leading to larger entanglement for the ground state (see Supplemental Material [39] for de- tails). The calculation of dynamical quantities is certainly a challenge and even the static expectation values have to be carefully analyzed with regards to the number of states kept (here $M = 1000$ states are used). As a consequence, the results presented for the two-orbital two-leg ladder below may not be as accurate as those for the chains.

On a ladder, there are two separate contributions to the SSF arising from the bonding ($q_y = 0$) and antibonding ($q_y = \pi$) sectors. For the two-orbital two-leg ladder results, presented in Fig. 7(b), we find a $q_y = 0$ dispersive mode at low-ω, with a continuum of spin excitations similar to the acoustic mode of the chain geometry. At $\omega \simeq 0.075\,$eV we find an energy narrow $q_y = \pi$ mode. According to our analysis of the 1D system, a similar spectrum can be found in the J_1-J_2 model on the ladder with FM rung coupling $J_\perp = J_1$, see Fig. 7(d). Both the J_1-J_2 spin model and multi-orbital model on the ladder studied here exhibit the 2×2 block state, i.e. AFM coupled blocks of four FM aligned spins on two neighbouring rungs [see Fig. 7(a)]. Such a state has a peak in the static SSF at $q_x = \pi/2$ in the bonding contribution ($q_y = 0$), see Fig. 7(c). Note that the maximum of the acoustic mode appear at $\omega \neq 0$, which suggests a non-zero spin gap, common in ladders. Finally, at higher frequencies ($\omega \simeq 0.13\,$eV) in the $q_y = 0$ sector we find a flat mode of excitations, similar to the optical mode present in the chain analysis. It is again evident that the latter is not captured by the J_1-J_2 model.

DISCUSSION

Let us compare the INS data for $BaFe_2Se_3$ reported in Ref. 22 against our results. Note that this compound is insulating [19], while our system Eqs. (1-2) for the parameters considered in this work, $U/W = 0.8$ and $J_H/U = 1/4$, is a (bad) metal in the block-OSMP phase, becoming insulator only for $U/W \gtrsim 1.5$ in the ferromagnetic-OSMP phase [47]. Considering that we have not included the three dimensionality of the system, crucial for transport, this discrepancy is not worrysome, particularly since our focus is magnetism. Within the spin-wave theory the low-ω portion of the INS spectra was interpreted [22] as a dispersive mode which reflects the frustrated nature of the $\pi/2$-order. In addition, the high-energy optical modes were interpreted as local excitation of spins within the 2×2 plaquette. A similar rationale was used to explain the INS result of the doped compound $Rb_{0.89}Fe_{1.58}Se_2$ [32]. Note that within the considered spin models of Ref. 22 and 32 large unphysical [48, 49] dimerization spin exchange couplings were required to stabilize the $\pi/2$ pattern.

From the perspective of our results, the interpretation of the INS spin spectra of low-dimensional ladder iron chalcogenides is different from spin-wave theory. The latter assumes that all excitations occur between localized spins, while in our system we have a mixture of localized and itinerant electrons. Moreover, as shown above, the SSF of multi-orbital systems not only contains dispersive acoustic modes but also local excitations controlled by the Hund exchange, at least within the block-OSMP. The inter-orbital nature of such modes cannot be properly captured by localized Heisenberg models. Our results, on both chain and ladder geometries, indicate that

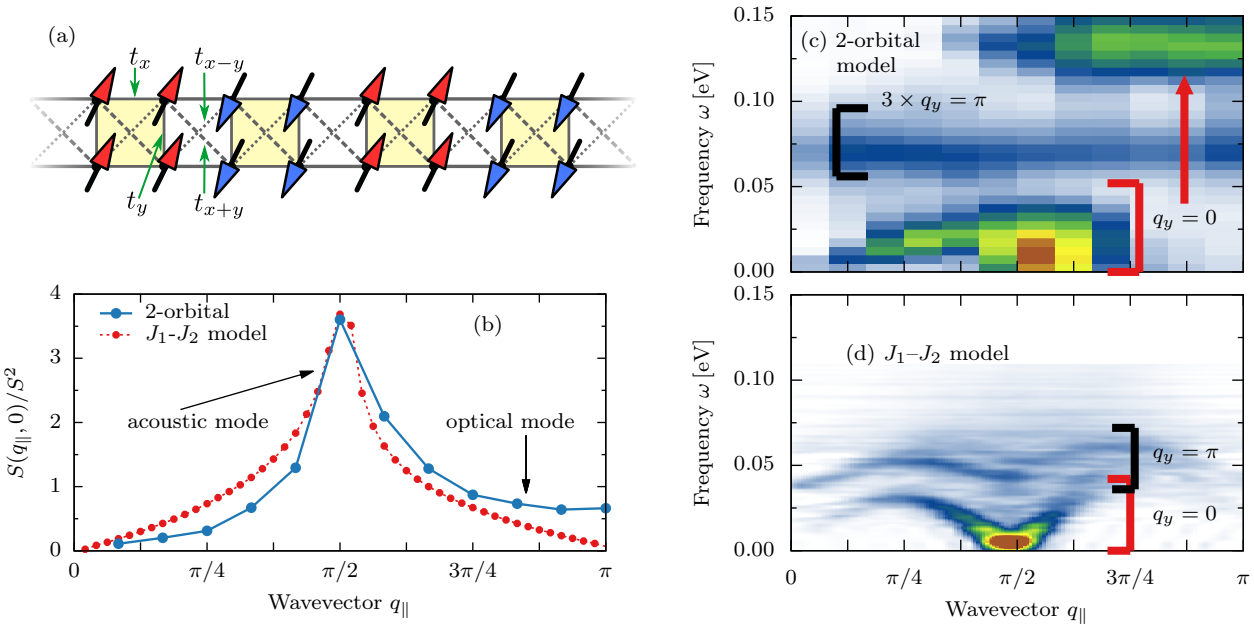

Figure 7. **Spin dynamics within the ladder geometry.** (a) Schematic representation of the two-orbital two-leg ladder system used in our analysis (see Methods section for details). Arrows depict the 2×2 block state. (b) Static SSF in the $q_y = 0$ sector for both the J_1-J_2 and multi-orbital models on a ladder geometry. (c,d) Dynamical SSF of the (c) two-orbital and (d) J_1-J_2 spin models on a two-leg ladder geometry (using $L = 12$ and $L = 48$ rungs, respectively).

spin models can only properly capture dispersive modes resulting from the peculiar spin order of a given phase as in the $\pi/2$ state of $BaFe_2Se_3$. However, we argue that only one of the low lying optical modes of this compound arises from a weakly dispersive (probably beyond experimental resolution of powder sample) $q_y = \pi$ excitation. Within our interpretation of the SSF spectra, the second optical mode is of a different nature, involving inter-orbital spin fluctuations on each site. Such a picture is consistent with our multi-orbital ladder results.

In conclusion, we have investigated the dynamical spin structure factor of a one-dimensional three-orbital Hubbard model in the block orbital selective Mott phase, as well as a ladder two-orbital Hubbard model also in a similar block state. This has been a computationally demanding effort even with the powerful DMRG, and to our knowledge this is the first time that results of this quality are produced. We have shown that our Hamiltonian captures nontrivial features of a broad family of low-dimensional iron chalcogenides, in particular for the ladder $BaFe_2Se_3$ compound for which $\pi/2$–block order was reported. We have found two different types of modes in the spin spectra: (i) low-frequency dispersive (acoustic) spin excitations and (ii) optical dispersionless excitations at higher energy. The acoustic band reflects the nature of magnetic order of the system, namely for the block-OSMP the frustrated $\pi/2$-ordering can be captured by the quantum J_1-J_2 frustrated Heisenberg model, as also shown here. The optical band arises from on-site inter-orbital spin fluctuations controlled by the Hund exchange coupling. Finally, our 1D dynamical SSF is in qualitative agreement with the INS spectrum of $BaFe_2Se_3$ [39]. Although the latter has only a quasi-1D geometry, with small but nonzero couplings perpendicular to the ladder, the ω dependent spectra should be dominated by the predominantly 1D nature of the system. As a consequence, the location in momentum and energy space is properly resolved by our model Hamiltonian Eqs. (1-2) for both of the modes.

Our results are general and should apply to a variety of block states in multi-orbital quasi-1D systems. They should all contain an acoustic band (with pitch wavevector compatible with the size of the magnetic block), a strong asymmetry in the distribution of weight of this acoustic band in different portions of the Brillouin zone, and optical modes with at least one of them related to atomic transitions regulated by the Hund coupling.

METHODS

DMRG method. The Hamiltonians discussed here were studied using primarily the density matrix renormalization group (DMRG) method [50, 51] within the single-center site approach [52], where the dynamical correlation functions are evaluated via the dynamical-DMRG [53, 54, 56] i.e. calculating spectral functions directly in frequency space with the correction-vector

method [55] with Krylov decomposition [56]. The computer package DMRG++ developed at ORNL was used. For a chain geometry, in both stages of the DMRG algorithm, we keep up to $M = 800$ states. This allow us to simulate accurately system sizes up to $L = 24$ sites for dynamical quantities (truncation $< 10^{-8}$ for all frequencies ω) and $L = 32$ for static quantities (truncation $< 10^{-10}$ for the GS). For the ladder geometry results, we use a standard two-site central block approach with $M = 1000$ states (truncation $< 10^{-3}$, showing that the two-leg ladder two-orbital results are qualitative, because of its close resemble to the rest, but their quantitative accuracy can be further improved in future efforts). In the Supplement [39] we present the scaling of our results with system size L, number of states kept M, and broadening η of Eq. (5).

Dynamical SSF. The zero temperature, $T = 0$, total spin structure factor (SSF) $S(q, \omega)$ is defined as:

$$S(q,\omega) = \frac{1}{\pi}\sqrt{\frac{2}{L+1}}\sum_{\ell=1}^{L}\sin(q\ell)\sin(qL/2)\times \\ \mathrm{Im}\,\langle \mathrm{GS}|\tilde{S}_\ell \frac{1}{\omega^- - (H-\epsilon_{\mathrm{GS}})}\tilde{S}_{L/2}|\mathrm{GS}\rangle\,, \quad (5)$$

with $\omega^- = \omega - i\eta$, and $|\mathrm{GS}\rangle$ is the ground state with energy ϵ_{GS}. In the above equation $\tilde{S}_\ell = \sum_\gamma S_{\ell,\gamma}$ is the total spin on site ℓ for the total SSF $S(q, \omega)$, or $\tilde{S}_\ell = \tilde{S}_{\ell,\gamma}$ for the orbital resolved SSF $S_{\gamma\gamma'}(q, \omega)$.

Furthermore, in the above equation we adopted the wave-vector definition appropriate for open boundary conditions (OBC), i.e. $q = k\pi/(L+1)$ with $k = 1, \ldots, L$. As a consequence, in this work we used approximate (exact in the thermodynamic limit $L \to \infty$) values of the wave-vectors, e.g., $q = \pi \equiv \pi L/(L+1)$.

Localized basis representation. The eigenstates $|\phi\rangle$ of the three orbital system can be written as

$$|\phi\rangle = \sum_{n=1}^{64^L} c_n |n\rangle \\ = \sum_{n_0=1}^{4^L}\sum_{n_1=1}^{4^L}\sum_{n_2=1}^{4^L} c(n_0,n_1,n_2)\,|n_0\rangle\otimes|n_1\rangle\otimes|n_2\rangle\,, (6)$$

where $|n\rangle$ represent the orthonormal basis (particle configuration) of all orbitals and $|n_\gamma\rangle$ (with $\gamma = 0, 1, 2$) represents the particle configuration on given orbital γ. Note that $\sum_n c_n^2 = \sum_{n_1,n_2,n_3} c^2(n_1, n_2, n_3) = 1$ and $\langle n_\gamma | n'_{\gamma'}\rangle = \delta_{nn'}\delta_{\gamma\gamma'}$. One can rewrite the above equation as

$$|\phi\rangle = \sum_{j=1}^{4^L} |\tilde{c}_j\rangle \otimes |j\rangle_{\gamma=2}\,, \quad (7)$$

where $j \equiv n_2$ represents - within OSMP - the localized orbital and

$$|\tilde{c}_j\rangle = \sum_{n_0=1}^{4^L}\sum_{n_1=1}^{4^L} c(n_0,n_1,n_2)\,|n_0\rangle\otimes|n_1\rangle \quad (8)$$

are vectors. The set of $\{|\tilde{c}_j\rangle\}$ vectors represent an orthogonal vector-space with $\sum_j \langle\tilde{c}_j|\tilde{c}_j\rangle = 1$. Finally, the weight of the $|j\rangle_{\gamma=2}$ configuration in the $|\phi\rangle$ eigenstate is given by the norm of the $|\tilde{c}_j\rangle$ vector, i.e., $\langle\tilde{c}_j|\tilde{c}_j\rangle = ||\tilde{c}_j|| \equiv \tilde{c}_j^2$.

Energy contribution. In Table I we present the expectation values of the several terms present in the Hamiltonian Eqs. (1-2) for the ground state and also states which contribute to the acoustic and optical modes.

Table I. **Energy contributions.** Kinetic, intra- and inter-orbital interaction, Hund, and pair-hopping energy contributions to the energy of given eigenstates. The last column shows the difference between $|\mathrm{GS}\rangle$ and states within the acoustic (red color) and optical (green color) modes. Results are obtained for $L = 4$ and $U/W = 0.8$, using the Lanczos method. All numbers in units of eV.

	ϵ_{k}	ϵ_{U}	$\epsilon_{\mathrm{U}'}$	ϵ_{H}	ϵ_{P}	Total	ω_α
$\|\mathrm{GS}\rangle$	−0.027	8.006	15.280	−1.055	−0.010	22.194	
$\|\mathrm{A}\rangle$	0.007	7.993	15.280	−1.065	−0.009	22.206	0.012
$\|\mathrm{O}\rangle$	−0.031	8.081	15.262	−0.946	−0.016	22.350	0.156

Two-orbital two-leg ladder Hamiltonian. The symmetric hoppings for the two-orbital two-leg ladder system are defined [34] in orbital space as follows [see sketch in Fig. 7(a)]:

$$t_x = \begin{pmatrix} 0.14769 & 0 \\ 0 & 0.27328 \end{pmatrix}, \qquad t_y = \begin{pmatrix} 0.28805 & 0.01152 \\ 0.01152 & 0.00581 \end{pmatrix},$$

$$t_{x\pm y} = \begin{pmatrix} -0.21166 & \mp 0.08430 \\ \mp 0.08430 & -0.18230 \end{pmatrix},$$

all expressed in units of eV. The interaction portion of the Hamiltonian is the same as in the 1D system Eq. (2).

* jherbryc@utk.edu

[1] For reviews on neutron scattering in cuprates see: J. Tranquada, H. Woo, T. Perring, H. Goka, G. Gu, G. Xu, M. Fujita, and K. Yamada, J. Phys. Chem. Solids **67**, 511 (2006), D. J. Scalapino, Rev. Mod. Phys. **84**, 1383 (2012), E. Fradkin, S. A. Kivelson, and J. M. Tranquada, Rev. Mod. Phys. **87**, 457 (2015), and E. Dagotto, Rev. Mod. Phys. **66**, 763 (1994).

[2] D. N. Basov and A. V. Chubukov, Nat. Phys. **7**, 272 (2011).

[3] M. Daghofer, A. Nicholson, A. Moreo, and E. Dagotto, Phys. Rev. B **81**, 014511 (2010), and references therein.

[4] R. M. Fernandes and A. V. Chubukov, Rep. Prog. Phys. **80**, 014503 (2017).

[5] Z. P. Yin , K. Haule, and G. Kotliar, Nat. Mat. **10**, 932 (2010).
[6] M. D. Lumsden and A. D. Christianson, J. Phys.: Condens. Matter **22**, 203203 (2010).
[7] P. Dai, J. Hu, and E. Dagotto, Nature Phys. **8**, 709 (2012).
[8] E. Dagotto, Rev. Mod. Phys. **85**, 849 (2013).
[9] W. Li, C. Setty, X. H. Chen, and J. Hu, Front. Phys. **9**, 465 (2014).
[10] E. Bascones, B. Valenzuela, and M. J. Calderón, C. R. Physique **17**, 36 (2016).
[11] E. Dagotto and T. M. Rice, Science **271**, 618 (1996), and references therein.
[12] K. Takubo, Y. Yokoyama, H. Wadati, S. Iwasaki, T. Mizokawa, T. Boyko, R. Sutarto, F. He, K. Hashizume, S. Imaizumi, T. Aoyama, Y. Imai, and K. Ohgushi, Phys. Rev. B **96**, 115157 (2017).
[13] T. Yamauchi, Y. Hirata, Y. Ueda, and K. Ohgushi, Phys. Rev. Lett. **115**, 246402 (2015).
[14] H. Takahashi, A. Sugimoto, Y. Nambu, T. Yamauchi, Y. Hirata, T. Kawakami, M. Avdeev, K. Matsubayashi, F. Du, C. Kawashima, H. Soeda, S. Nakano, Y. Uwatoko, Y. Ueda, T. J. Sato, and K. Ohgushi, Nat. Mater. **14**, 1008 (2015).
[15] J. Ying, H. Lei, C. Petrovic, Y. Xiao, and V.V. Struzhkin, Phys. Rev. B **95**, 241109(R) (2017).
[16] Y. Zhang, L.-F. Lin, J.-J. Zhang, E. Dagotto, and S. Dong, Phys. Rev. B **97**, 045119 (2018).
[17] M. Uehara, T. Nagata, J. Akimitsu, H. Takahashi, N. Mori, and K. Kinoshita, J. Phys. Soc. Jpn. **65**, 2764 (1996).
[18] A. Georges, L. d. Medici, and J. Mravlje, Annu. Rev. Condens. Matter Phys. **4**, 137 (2013), and references therein.
[19] J. M. Caron, J. R. Neilson, D. C. Miller, K. Arpino, A. Llobet, and T. M. McQueen, Phys. Rev. B **85**, 180405 (2012).
[20] J. Rincón, A. Moreo, G. Alvarez, and E. Dagotto, Phys. Rev. Lett. **112**, 106405 (2014).
[21] S. Dong, J.-M. Liu, and E. Dagotto, Phys. Rev. Lett. **113**, 187204 (2014).
[22] M. Mourigal, S. Wu, M.B. Stone, J.R. Neilson, J.M. Caron, T.M. McQueen, and C.L. Broholm, Phys. Rev. Lett. **115**, 047401 (2015).
[23] M. Wang, S. J. Jin, Ming Yi, Yu Song, H. C. Jiang, W. L. Zhang, H. L. Sun, H. Q. Luo, A. D. Christianson, E. Bourret-Courchesne, D. H. Lee, Dao-Xin Yao, and R. J. Birgeneau, Phys. Rev. B **95**, 060502(R) (2017).
[24] M. Wang, M. Yi, S. Jin, H. Jiang, Y. Song, H. Luo, A. D. Christianson, C. de la Cruz, E. Bourret-Courchesne, D.-X. Yao, D. H. Lee, and R. J. Birgeneau, Phys. Rev. B **94**, 041111(R) (2016).
[25] S. Chi, Y. Uwatoko, H. Cao, Y. Hirata, K. Hashizume, T. Aoyama, and K. Ohgushi, Phys. Rev. Lett. **117**, 047003 (2016).
[26] T. Hawai, Y. Nambu, K. Ohgushi, F. Du, Y. Hirata, M. Avdeev, Y. Uwatoko, Y. Sekine, H. Fukazawa, J. Ma, S. Chi, Y. Ueda, H. Yoshizawa, and T. J. Sato, Phys. Rev. B **91**, 184416 (2015).
[27] Y. Nambu, K. Ohgushi, S. Suzuki, F. Du, M. Avdeev, Y. Uwatoko, K. Munakata, H. Fukazawa, S. Chi, Y. Ueda, and T. J. Sato, Phys. Rev. B **85**, 064413 (2012).
[28] J. M. Caron, J. R. Neilson, D. C. Miller, A. Llobet, and T. M. McQueen, Phys. Rev. B **84**, 180409(R) (2011).
[29] J. Guo, S. Jin, G. Wang, S. Wang, K. Zhu, T. Zhou, M. He, and X. Chen, Phys. Rev. B **82**, 180520(R) (2010).
[30] Z. Shermadini, A. Krzton-Maziopa, M. Bendele, R. Khasanov, H. Luetkens, K. Conder, E. Pomjakushina, S. Weyeneth, V. Pomjakushin, O. Bossen, and A. Amato, Phys. Rev. Lett. **106**, 117602 (2011).
[31] F. Ye, S. Chi, Wei Bao, X. F. Wang, J. J. Ying, X. H. Chen, H. D. Wang, C. H. Dong, and M. Fang, Phys. Rev. Lett. **107**, 137003 (2011).
[32] M. Wang, C. Fang, D.-X. Yao, G. Tan, L. W. Harriger, Y. Song, T. Netherton, C. Zhang, M. Wang, M. B. Stone, W. Tian, J. Hu, and P. Dai, Nat. Comm. **2**, 580 (2011).
[33] B. Wei, H. Qing-Zhen, C. Gen-Fu, M. A. Green, W. Du-Ming, H. Jun-Bao, and Q. Yi-Ming, Chin. Phys. Lett. **28**, 086104 (2011).
[34] Q. Luo, A. Nicholson, J. Rincn, S. Liang, J. Riera, G. Alvarez, L. Wang, W. Ku, G. D. Samolyuk, A. Moreo, and E. Dagotto, Phys. Rev. B **87**, 024404 (2013).
[35] K. Haule and G. Kotliar, New J. Phys. 11, 025021 (2009).
[36] Q. Luo, G. Martins, D.-X. Yao, M. Daghofer, R. Yu, A. Moreo, and E. Dagotto, Phys. Rev. B **82**, 104508 (2010).
[37] J. Rincón, A. Moreo, G. Alvarez, and E. Dagotto, Phys. Rev. B **90**, 241105(R) (2014).
[38] N. Kaushal, J. Herbrych, A. Nocera, G. Alvarez, A. Moreo, F. A. Reboredo, and E. Dagotto, Phys. Rev. B. **96**, 155111 (2017).
[39] See Supplemental Material for: (i) details of numerical calculations and (ii) comparison of 1D DMRG results with $BaFe_2Se_3$ experiments.
[40] A. Nicholson, Q. Luo, W. Ge, J. Riera, M. Daghofer, G. B. Martins, A. Moreo, and E. Dagotto, Phys. Rev. B **84**, 094519 (2011).
[41] M. Enderle, B. Fåk, H.-J. Mikeska, R. K. Kremer, A. Prokofiev, and W. Assmus, Phys. Rev. Lett. **104**, 237207 (2010).
[42] J. Ren and J. Sirker, Phys. Rev. B **85**, 140410(R) (2010).
[43] H. Onishi, J. Phys. Soc. Jpn. **84**, 083702 (2015).
[44] H. Onishi, J. Phys.: Conf. Ser. **592**, 012109 (2015).
[45] R. Bursill, G. A. Gehring, D. J. J. Farnell, J. B. Parkinson, T. Xiang, and C. Zeng, J. Phys.: Condens. Matter **7**, 8605 (1995).
[46] It should be pointed out that using a small $L = 4$ system with OBC we have found another state which contributes to the optical mode, i.e., $|\widetilde{O}\rangle_{\gamma=2} = 1/2(|\downarrow\uparrow\downarrow\uparrow\rangle_{\gamma=2} + |\uparrow\downarrow\uparrow\downarrow\rangle_{\gamma=2})$. However, such a state is not present in the system with periodic boundary conditions.
[47] S. Li, N. Kaushal, Y. Wang, Y. Tang, G. Alvarez, A. Nocera, T. A. Maier, E. Dagotto, and S. Johnston, Phys. Rev. B **94**, 235126 (2016).
[48] J.-K. Bao, C.-M. Feng, Y.-K. Luo, H. Jiang, Y.-L. Sun, W.-H. Jiao, C.-Y. Shen, Z.-A. Xu, and G.-H. Cao, J. of Phys.: Cond. Matt. **26**, 026002 (2014).
[49] Z. V. Popović, M. Šcepanović, N. Lazarević, and M. Opačić, M. M. Radonjić, and D. Tanasković, Phys. Rev. B **91**, 064303 (2015).
[50] S. R. White, Phys. Rev. Lett. **69**, 2863 (1992).
[51] U. Schollwöck, Rev. Mod. Phys. **77**, 259 (2005).
[52] S. R. White, Phys. Rev. B **72**, 180403 (2005).
[53] E. Jeckelmann, Phys. Rev. B **66**, 045114 (2002).
[54] H. Benthein and E. Jackelmann, Phys. Rev. B **75**, 205128 (2007).
[55] T. D. Kühner and S. R. White, Phys. Rev. B **60**, 335 (1999).

[56] A. Nocera and G. Alvarez, Phys. Rev. E **94**, 053308 (2016).

ACKNOWLEDGMENTS

J.H, A.M., and E.D. were supported by the US Department of Energy (DOE), Office of Basic Energy Sciences (BES), Materials Sciences and Engineering Division. N.K. was supported by the National Science Foundation Grant No. DMR-1404375. The work of G.A. was conducted at the Center for Nanophase Materials Science, sponsored by the Scientific User Facilities Division, BES, DOE, under contract with UT-Battelle.

SUPPLEMENTARY MATERIAL for:
"Spin dynamics of the block orbital-selective Mott phase" by J. Herbrych *et al.*

Numerical details

In Fig. S1 we present the parameter dependence of our dynamical-DMRG calculations for a fixed frequency $\omega = 0.03\,[\mathrm{eV}]$ (namely, "inside" the acoustic mode) and $L = 16$ sites (48 orbitals). In panel (a) we present the broadening η dependence of our calculations [Eq. (4) of the main text]. It is clear from the figure that all features are properly resolved for the considered $\eta/\delta\omega = 2$. In Fig. S1(b) we present the number of states kept M dependence of our findings. We conclude that at a fixed η and L, the results do not change appreciably for $M \gtrsim 800$.

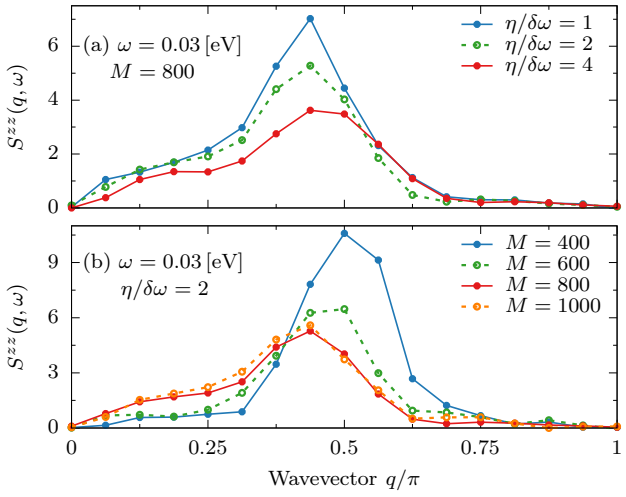

Figure S1. **Parameter dependence of dynamical-DMRG simulations.** (a) Broadening η and (b) number of states kept M dependence corresponding to $\omega = 0.03\,[\mathrm{eV}]$ and $L = 16$ sites. In all simulations of the main text we use $\eta/\delta\omega = 2$ and $M = 800$.

In Fig. S2(a-c) we present the finite-size analysis at several momenta q cuts through the dynamical SSF. At large $q/\pi = 3/4$, the results do not depend on the system size L because for this momentum only the optical mode is present in the spectrum. Since the excitations within this mode are local, the system size (and also dimensionality of the lattice) should not play a crucial role. On the other hand, at $q \leq \pi/2$ the results depend more on the system size with maximal variation at $q/\pi = 1/2$. However, this dependence does not change the main findings of our work and it merely reflects the quasi-long-range nature of the block ordering [S1]. This can be understood simply from the L-scaling of the static $S(q = \pi)$ shown in the inset of Fig. S2(d). For completeness in Fig. S2(d) we show the L dependence of the full momentum q resolved static SSF.

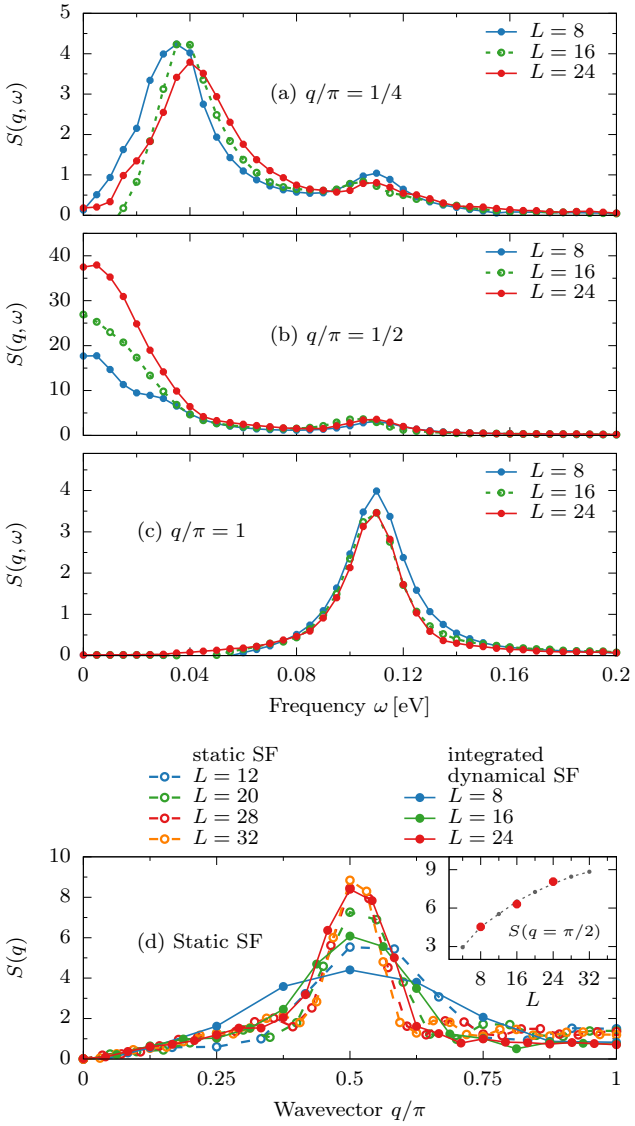

Figure S2. **Finite-size analysis.** (a-c) Size L dependence of the frequency-resolved dynamical SSF for $q/\pi = 1/4, 1/2, 3/4$, as calculated with $\eta/\delta\omega = 2$ and $M = 800$. (d) L-dependence of the static SSF. Open points represent the results obtained as the expectation value of the GS, while solid points are obtained from the integral over the frequency (see main text for details). Inset illustrates the quasi-long-range nature of block $\pi/2$ ordering, with a signal intensity growing with L.

Let us finally comment on the accuracy of our results for the multi-orbital ladder geometry. Different from the chain setup, where the three orbitals where treated as a single site with a local Hilbert space of 64 states, the ladder results were obtained using a $12 \times 2 \times 2$ (rungs $\times$ legs $\times$ orbitals) lattice with a local Hilbert space of 4 states. Although such a setup have smaller memory requirements, the entanglement area law [S5] heavily influences the accuracy of our results. The latter is a consequence of a large number of long-range connections (up

to 7 nearest-neighbours). In Fig. S3, we present the system size L and states M scaling of the results presented in Fig. 7 of the main text. In panel (a) we present the finite-size analysis of the static SSF in the bonding sector, $q_y/\pi = 0$, for the $M = 1000$ states kept. The system size analysis of the ladder results is consistent with the findings for chains, namely the acoustic mode has size dependence, while the optical mode does not. In summary, while we are confident that our results for ladders capture the essence of the problem, including the existence of acoustic and optical bands and quite different weights in different portions of the Brillouin zone, only further (very demanding) work can achieve the same accuracy as shown here for chains.

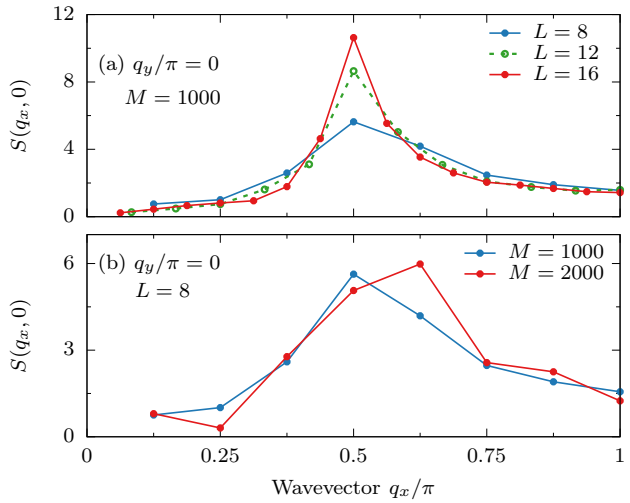

Figure S3. **Ladder geometry analysis.** (a) Finite size L and (b) number of states kept M scaling of the static SSF in the bonding sector, $q_y/\pi = 0$.

Comparison of DMRG results with powder experiments.

Although $BaFe_2Se_3$ is a quasi-1D compound, the finite ω-dependent properties should be dominated by the 1D nature of the ladder lattice (while, e.g., d.c. transport is more subtle). It is therefore appropriate to directly compare our dynamical SSF to experimental findings. Since the latter is obtained using a powder sample, our results presented in Fig. 2 of the main text have to be averaged over all spherical angles [S2]. Furthermore, to qualitatively compare to the inelastic neutron scattering (INS) data we must incorporate in the analysis the momentum dependent magnetic form factors $F(Q)$ of the spin carriers, namely the Fe^{2+} ions. Here we assume a gyromagnetic ratio $g = 2$ (spin-only scattering). The functional form of the former can be taken from crystallography tables [S3]. In Fig. S4(a) we present the powder average of our spectra. Several interesting general features can be inferred: (i) using realistic values [S4] for the Fe-Fe distance such as 2.7 Å, remarkably we obtain a nearly perfect agreement for the position of the acoustic mode. The leading INS signal is centered at $Q \simeq 0.7$ (1/Å) followed by a gradual decay in ω and increase in intensity culminating in the range 1.8 (1/Å) to 2.5 (1/Å) [indicated by vertical red arrows in Fig. S4(b)]. (ii) The neutron spectrum gives three flat (momentum-independent) bands of spin exactions: two of them are centered approximately at $\omega \sim 0.1$ eV ($\omega_1 = 0.0889$ eV and $\omega_2 = 0.1082$ eV, depicted as horizontal red arrows in Fig. S4(b)), while the third one is positioned at $\omega_3 = 0.198$ eV. Our 1D results yield only one optical mode centered at $\omega \simeq 0.105$ eV in accord with the most pronounced peak within the INS spectrum. This qualitative agreement indicates that our model is able to capture the nontrivial nature of the frustrated magnetism of $BaFe_2Se_3$, and that the studied parameter range of our Hamiltonian is valid for the whole 123 family.

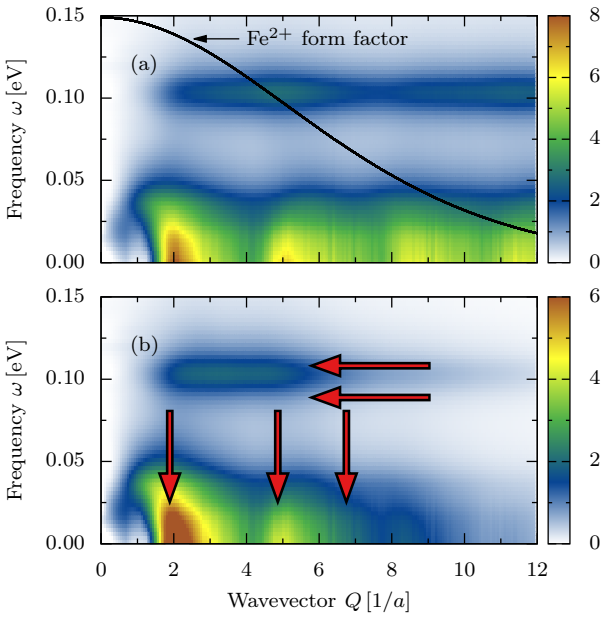

Figure S4. **Powder spectrum.** (a) Spherical average of the dynamical SSF. The black solid line represents the magnetic form factor $F(Q)^2$ of the Fe^{2+} ions [S3]. (b) Spherical average of the dynamical SSF convoluted with the form factor $F(q)$ relevant for a direct comparison with the $BaFe_2Se_3$ INS results [S4]. Red arrows indicate the position of maximum intensities in the INS spectrum. See text for details.

* jherbryc@utk.edu

[S1] J. Rincón, A. Moreo, G. Alvarez, and E. Dagotto, Phys. Rev. Lett. **112**, 106405 (2014).

[S2] K. Tomiyasu, M. Fujita, A. I. Kolesnikov, R. I. Bewley, M. J. Bull, and S. M. Bennington, Appl. Phys. Lett. **94**, 092502 (2009).

[S3] P. J. Brown, Magnetic Form Factors, Chapter 4.4.5, International tables for crystallography vol. C (A. J. C. Wilson, ed.), pp. 391-399.

[S4] M. Mourigal, S. Wu, M.B. Stone, J.R. Neilson, J.M. Caron, T.M. McQueen, and C.L. Broholm, Phys. Rev. Lett. **115**, 047401 (2015).

[S5] *Strongly Correlated Systems - Numerical Methods*, edited by A. Avella and F. Mancini (Springer Series in Solid–State Sciences 176, Berlin, 2013).